electronics

MDPI

Article

Analysis and Implementation of a Frequency Control DC–DC Converter for Light Electric Vehicle Applications

Bor-Ren Lin

Department of Electrical Engineering, National Yunlin University of Science and Technology, Yunlin 640, Taiwan; linbr@yuntech.edu.tw

Abstract: In order to realize emission-free solutions and clean transportation alternatives, this paper presents a new DC converter with pulse frequency control for a battery charger in electric vehicles (EVs) or light electric vehicles (LEVs). The circuit configuration includes a resonant tank on the high-voltage side and two variable winding sets on the output side to achieve wide output voltage operation for a universal LEV battery charger. The input terminal of the presented converter is a from DC microgrid with voltage levels of 380, 760, or 1500 V for house, industry plant, or DC transportation vehicle demands, respectively. To reduce voltage stresses on active devices, a cascade circuit structure with less voltage rating on power semiconductors is used on the primary side. Two resonant capacitors were selected on the resonant tank, not only to achieve the two input voltage balance problem but also to realize the resonant operation to control load voltage. By using the variable switching frequency approach to regulate load voltage, active switches are turned on with soft switching operation to improve converter efficiency. In order to achieve wide output voltage capability for universal battery charger demands such as scooters, electric motorbikes, Li-ion e-trikes, golf carts, luxury golf cars, and quad applications, two variable winding sets were selected to have a wide voltage output (50~160 V). Finally, experiments with a 1 kW rated prototype were demonstrated to validate the performance and benefits of presented converter.

Keywords: pulse frequency modulation; light electric vehicle; wide output voltage

Citation: Lin, B.-R. Analysis and Implementation of a Frequency Control DC–DC Converter for Light Electric Vehicle Applications. *Electronics* **2021**, *10*, 1623. https://doi.org/10.3390/electronics10141623

Academic Editor: Nikolay Hinov

Received: 24 June 2021
Accepted: 6 July 2021
Published: 7 July 2021

1. Introduction

Clean renewable energies with power electronic techniques have been widely developed to generate alternative current (AC) voltage or direct current (DC) voltage on AC utility systems [1–4] or DC microgrid systems [5,6]. Normally, DC/DC pulse-width modulation converters (PWMs) and AC/DC PWM converters are adopted for solar power [7,8] and wind power [9] applications to convert unstable DC and AC voltage into a stable DC voltage on DC nanogrid or microgrid systems. The DC bus voltage on a DC microgrid may be 380, 760, or 1500 V for residential houses, light rail vehicles, or DC traction vehicles applications, respectively. DC–DC converters [10–13] with full bridge circuit topologies have been developed to convert low voltage (380 V) input into low voltage units (5, 12, or 48 V) for computers, server systems, light electric vehicle (LEVs), or telecommunication applications. Three level or multilevel converters [14–16] have been proposed for medium voltage (760 V) or high voltage (1500 V) input applications. Soft switching converters were researched in [17–22] to decrease switching losses on power semiconductors and high efficiency. Active clamp pulse-width modulation (PWM) and asymmetric PWM techniques were studied in [17,18] to improve the switching loss from half rated power to full power by adding an extra inductor on the primary side of a DC/DC PWM converter. However, the main problems of asymmetric PWM converters are unbalanced voltages and current stresses on power devices. Using the phase shift PWM technique on full bridge converters [19,20] can reduce switching loss and obtain a high circuit efficiency. The main disadvantage of phase shift PWM techniques is the hard switching problem on the lagging-leg switches. Resonant converters with the pulse frequency modulation technique were presented in [21,22] to realize low switching losses on power semiconductors over the whole load range. However, the main drawback of resonant converters is their narrow input voltage range.

To implement clean transportation alternatives and realize emission-free demands, a new PWM converter with the advantages of a wide voltage output capability and low switching loss is presented and verified in this paper for a universal battery charger in LEV or electric vehicle (EV) applications. A cascade resonant circuit was selected to lessen the voltage rating on active devices so that 600 V power switches are adopted for the 760 V input condition. Two resonant capacitors are used on the resonant tank to not only achieve resonant behavior but also input spilt voltage balance. Due to the variable switching frequency, active devices are turned on under zero voltage switching (ZVS), and the fast recovery diodes are turned off under zero current switching (ZCS). Therefore, the power losses are reduced in the presented converter. To implement the wide voltage output capability for universal battery charger applications in LEV or EV systems, two winding sets were selected for the low voltage side to have different voltage gains under high or low output voltage regions. The presented circuit has a more concise circuit configuration, less device counts, and an easier control strategy when using the general purpose PWM integrated circuit compared to the conventional DC converters. The basic DC microgrid system and the circuit configuration of the presented converter are provided in Section 2. The circuit operation for wide voltage operation capability is discussed in Section 3. The circuit analysis of the studied converter is provided in Section 4. Section 5 gives the design procedures and experiments of the presented circuit. In Section 6, the conclusion and future work directions are provided.

2. Circuit Configuration

The basic circuit blocks of DC nanogrid or microgrid systems are illustrated in Figure 1. The input voltages on a DC microgrid can be DC or AC voltage from clean renewable energies such as wind power and photovoltaic (PV) power or utility systems. Therefore, the AC/DC or DC/DC PWM converters need to change unstable AC voltage from wind turbine generators or unstable DC voltage from PV panels to stable DC voltage on DC microgrid systems. Bidirectional AC/DC or DC/DC PWM converters are needed between utility and DC microgrid systems to achieve bidirectional power flow capability. DC microgrids can supply AC motor drives, energy storage units, light rail transit systems, or battery chargers for LEVs through DC/AC inverters or DC/DC converters. The input voltage of DC transportation applications is 750 or 1500 V. However, the input voltage of a residential house or a local industry factory is 380, ±380, or 760 V. Therefore, the DC bus voltage on DC microgrids can be 380, ±380, 760, or 1500 V for different power rating requirements. High voltage PWM converters are normally adopted to supply the high power output for EV chargers or DC transportation systems.

Figure 2 provides a circuit diagram of the studied high voltage DC/DC converter. The input voltage is 760 V from the DC bus of the DC microgrid. The output voltage of the studied converter is used to charge batteries for LEV applications such as scooters, electric motorbikes, Li-ion e-trikes, golf carts, luxury golf cars, and quads. Due to the wide battery voltage range in LEV applications, DC/DC converters need to have wide output voltage operation capabilities. Figure 2a provides a diagram of the presented circuit with V_{in} = 760 V and V_o = 50 V–160 V. Four active devices, two input capacitors, an isolated transformer, a resonant inductor, and two resonant capacitors are used on the high voltage side (primary side). Four fast recovery diodes, an active switch, an output capacitor, and a DC resistor are adopted on the low voltage side (secondary side). Due to the series connection of four active devices on the high voltage side, active devices with a 600 V voltage rating are adopted on the primary side to withstand 760 V input. The series resonant circuit structure with L_r, C_{r1}, C_{r2}, and L_m is adopted on the presented converter to have the advantage of a soft switching operation for active devices (S_1–S_4) and fast recovery diodes (D_1–D_4). Two center-taped rectifiers with different winding turns are used on the low voltage side to extend the output voltage range operation. If switch S_5 is OFF (Figure 2b), D_1 and D_4 are OFF. The low voltage output is provided in the proposed converter with n_s secondary winding turns. The voltage gain at the low voltage output condition (Figure 2b) is $V_o/V_{in} = G(f_{sw})n_s/(4n_p)$, where $G(f_{sw})$ is the voltage gain of the series resonant circuit. If switch S_5 is ON (Figure 2c), D_2 and D_3 are OFF and the high voltage output is provided in the proposed converter with $2n_s$ secondary winding turns. Therefore, the voltage gain at the high voltage output condition is $V_o/V_{in} = G(f_{sw})n_s/(2n_p)$. Thus, the studied converter can provide a low (high) voltage output range with S_5 OFF (ON).

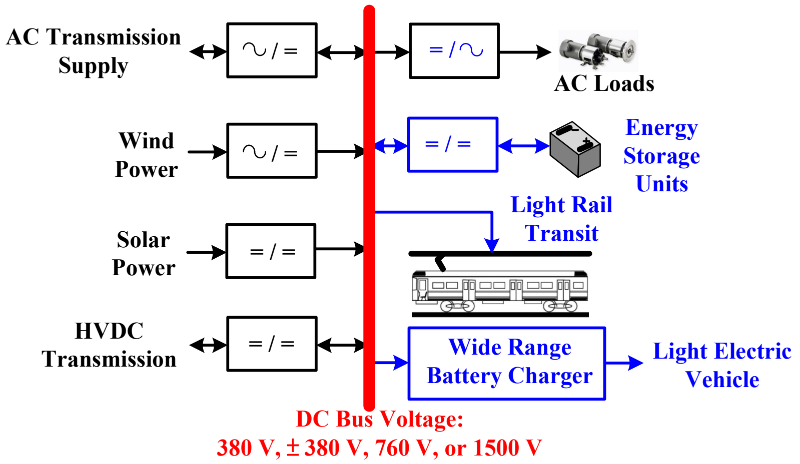

Figure 1. Circuit blocks of a simplified DC microgrid system.

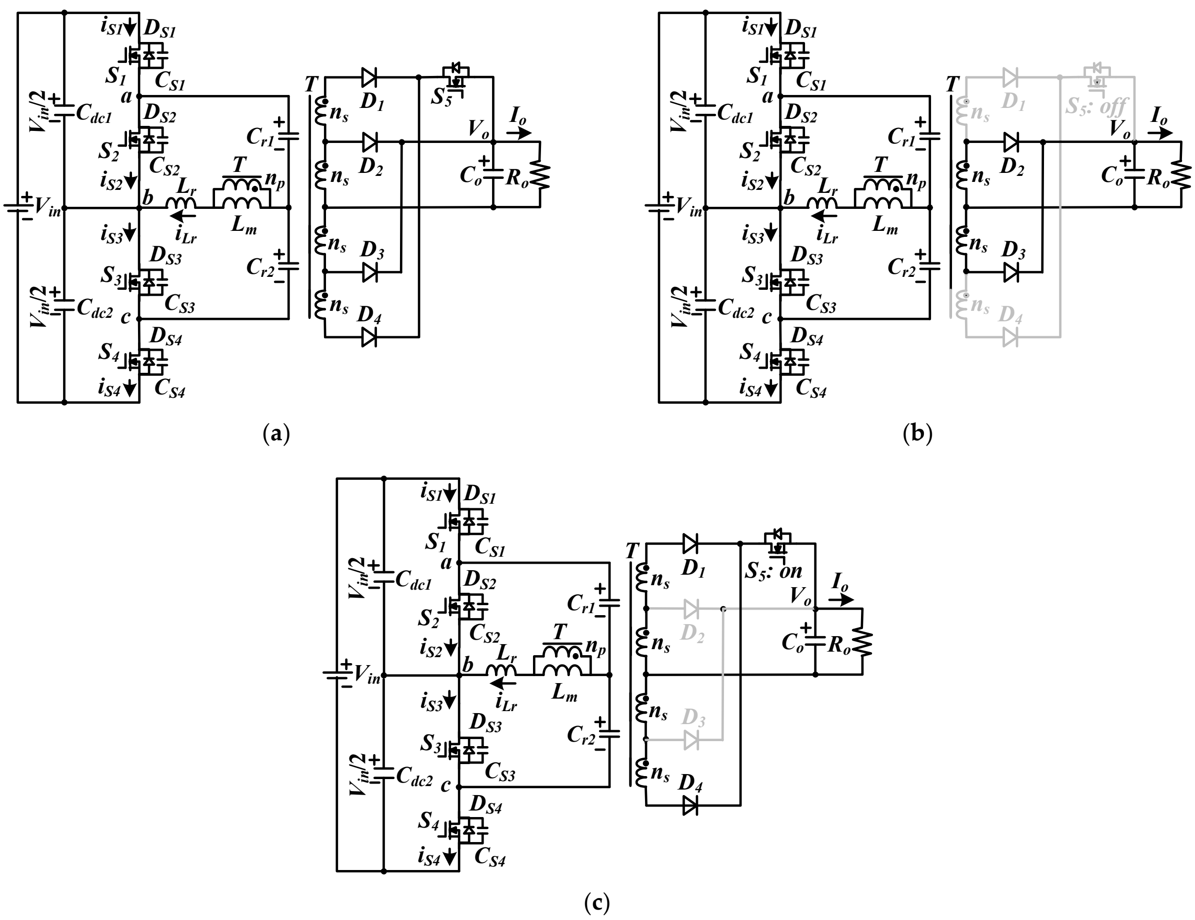

Figure 2. Circuit configuration of (**a**) presented DC/DC converter at (**b**) low voltage output and (**c**) high voltage output.

3. Circuit Operation

To realize the wide output voltage operation, the presented circuit has two equivalent sub-circuits, as shown in Figure 2b,c. S_1–S_4 are controlled with pulse switching frequency modulation (PFM). For low and high output voltage ranges, the switching signals and the main voltage and current waveforms are provided in Figure 3a,b, respectively. For the low voltage output range, the studied converter is only operated at a low voltage gain. Therefore, S_5 is off, and D_1 and D_4 are also off. In order to generate the square voltage PWM waveforms on leg voltages v_{ab} and v_{bc}, the gate waveforms of S_1 (S_2) and S_3 (S_4) are identical. If the proposed converter is used at the switching frequency f_{sw} < (or >) series resonant frequency $f_{r,1}$ by C_{r1}, C_{r2}, and L_r, the presented resonant converter has six (or four) working modes in every switching cycle. Figure 4 shows the equivalent working modes under $f_{sw} < f_{r,1}$. If the converter is operated at $f_{sw} > f_{r,1}$, then only modes 1, 3, 4, and 6 are used in the proposed converter for every switching period.

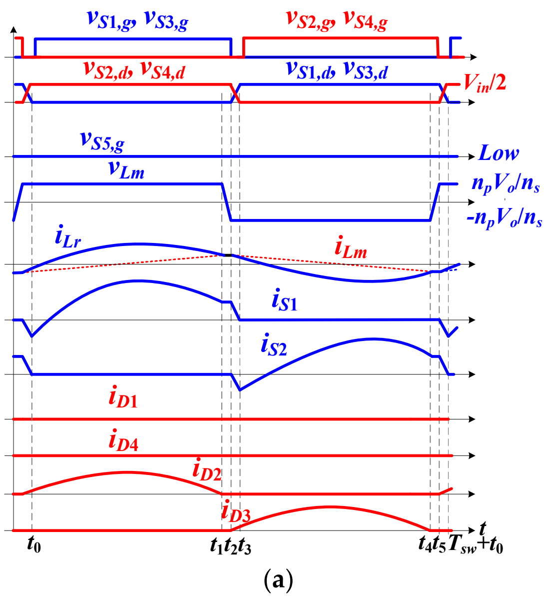

Figure 3. Main PWM signals and circuit waveforms of the presented converter for (**a**) the low output voltage range and (**b**) the high output voltage range.

Mode 1 [$t_0 \sim t_1$]: $v_{CS1} = v_{CS3} = 0$ at time t_0. Due to $i_{CS3} < 0$ and $i_{CS1} < 0$, the body diodes D_{S3} and D_{S1} are naturally conducting. The ZVS turn-on of S_3 and S_1 is accomplished at t_0. The capacitor voltage $v_{Cr2} + v_{Cr1} = V_{dc1}$. Due to $i_{Lr}(t) > i_{Lm}(t)$, the fast recovery diode D_2 is conducting and $v_{Lm} = (n_p/n_s)V_o$. L_r, C_{r2}, and C_{r1} are resonant in mode 1 with resonant frequency $f_{r,1} = 1/2\pi\sqrt{2L_rC_r}$ where $C_r = C_{r1} = C_{r2}$.

Mode 2 [$t_1 \sim t_2$]: since $f_{r,1} < f_{sw}$, i_{D2} will decrease to 0 at t_1. Then, D_1 becomes off without reverse recovery current loss. On the primary side, L_m, L_r, C_{r2}, and C_{r1} are naturally resonant with the resonant frequency $f_{r,2} = 1/2\pi\sqrt{2(L_r + L_m)C_r}$.

Mode 3 [$t_2 \sim t_3$]: S_1 and S_3 are turned off at t_2, and C_{S2} and C_{S4} are discharged. After time t_2, $i_{Lm} > i_{Lr}$ such that D_3 is conducting and v_{Lm} becomes $-(n_p/n_s)V_o$. The magnetizing current $i_{Lm}(t_2)$ can be obtained as follows:

$$i_{Lm}(t_2) \approx (n_pV_o)/(4n_sL_mf_{sw}) \quad (1)$$

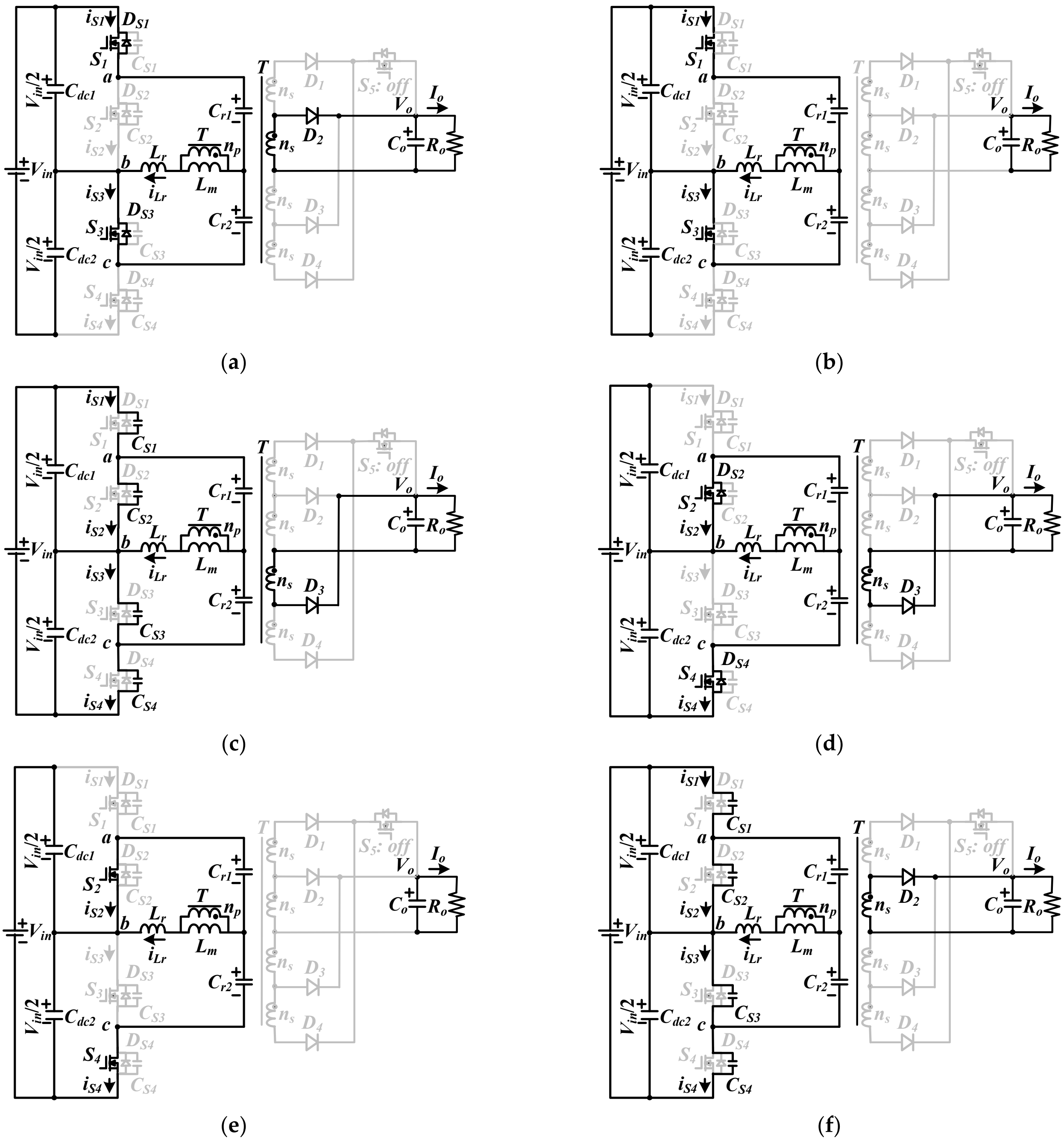

Figure 4. Equivalent mode circuits under low voltage range operation if $f_{sw} < f_r$: (**a**) mode 1 circuit, (**b**) mode 2 circuit, (**c**) mode 3 circuit, (**d**) mode 4 circuit, (**e**) mode 5 circuit, and (**f**) mode 6 circuit.

The ZVS condition of S_4 and S_2 is given as:

$$i_{Lm}(t_2) \geq V_{in}\sqrt{C_{oss}/(L_m + L_r)} \tag{2}$$

where C_{oss} = C_{S1} = C_{S2} = C_{S3} = C_{S4}. However, the dead time t_d between S_2 and S_1 must be greater than the discharged time of C_{S2} and C_{S4}. Therefore, the maximum value of L_m can be obtained as follows:

$$L_m \leq (n_p V_o t_d)/(4V_{in} f_{sw} n_s C_{oss}) \tag{3}$$

Mode 4 [t_3 ~ t_4]: at t_3, v_{CS2} = v_{CS4} = 0. The body diodes D_{S4} and D_{S2} are naturally forward-biased. The ZVS turn-on of S_4 and S_2 is achieved. Due to $i_{Lr}(t_3)$ < $i_{Lm}(t_3)$, the fast recovery diode D_3 is conducting and $v_{Lm} = -(n_p/n_s)V_o$. L_r, C_{r2}, and C_{r1} are naturally resonant on the primary side in mode 4.

Mode 5 [$t_4 \sim t_5$]: at time t_4, $i_{D3} = 0$. Thus, D_3 becomes off. L_m, L_r, C_{r2}, and C_{r1} are naturally resonant on the primary side with the resonant frequency $f_{r,2}$.

Mode 6 [$t_5 \sim T_{sw}+t_0$]: S_2 and S_4 turn off at t_5, and C_{S1} and C_{S3} are discharged. After time t_5, $i_{Lm} < i_{Lr}$ such that D_2 becomes forward-biased and $v_{Lm} = (n_p/n_s)V_o$. At time $t_0 + T_{sw}$, $v_{CS1} = v_{CS3} = 0$.

For the high voltage output range, the studied converter has a high voltage gain. S_5 is turned on, and the fast recovery diodes D_2 and D_3 are reverse-biased. The presented converter has six (or four) operating modes in every switching cycle if f_{sw} < (or >) $f_{r,1}$. Figure 5 provides the equivalent circuits for $f_{sw} < f_{r,1}$.

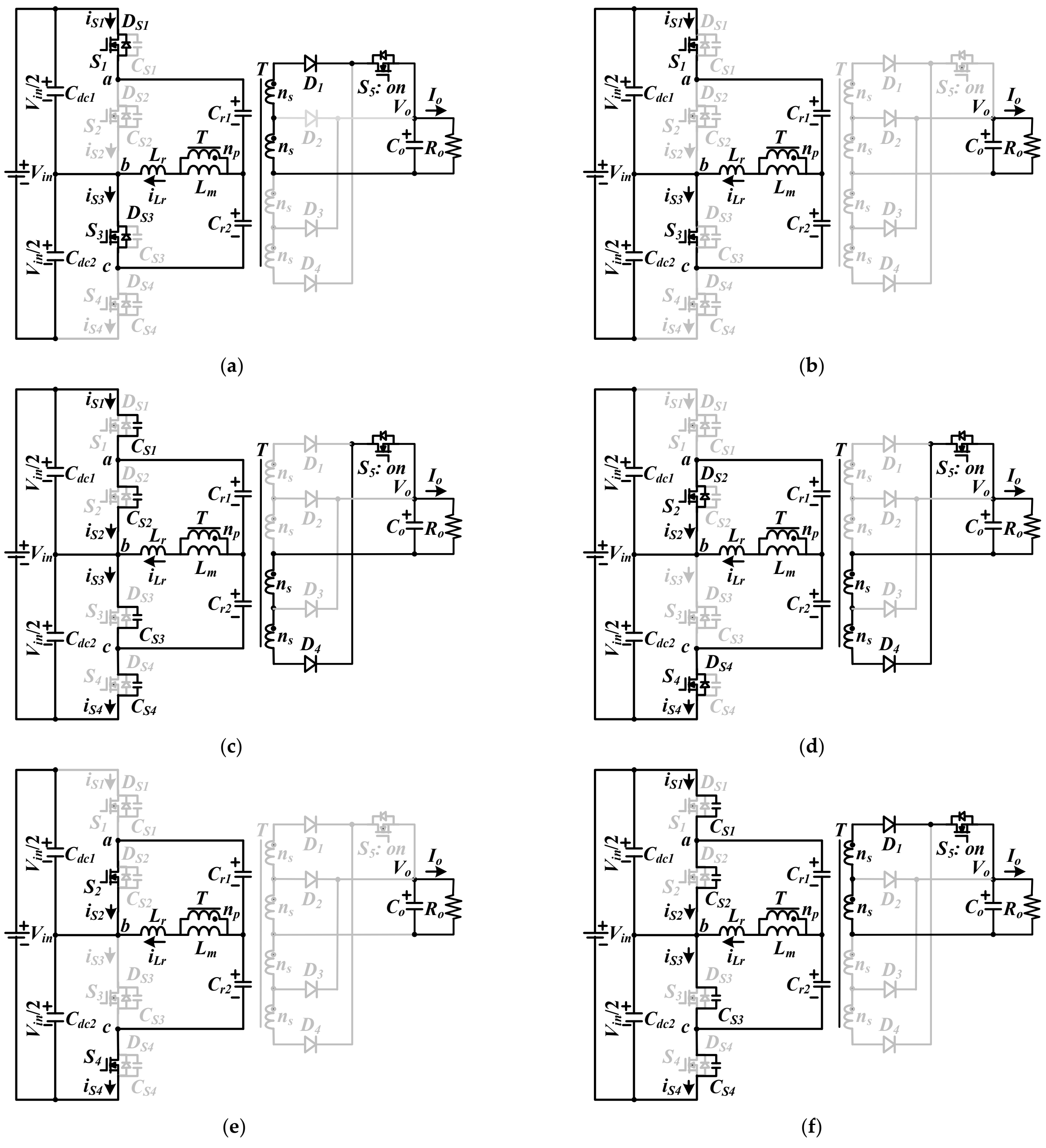

Figure 5. Equivalent mode circuits under high voltage range operation if $f_{sw} < f_r$: (**a**) mode 1 circuit, (**b**) mode 2 circuit, (**c**) mode 3 circuit, (**d**) mode 4 circuit, (**e**) mode 5 circuit, and (**f**) mode 6 circuit.

Mode 1 [t_0 ~ t_1]: at time t_0, v_{CS1} = v_{CS3} = 0. D_{S1} and D_{S3} are conducting, $v_{S2,ds}$ = $v_{S4,ds}$ = $V_{in}/2$, and v_{Cr1} + v_{Cr2} = $V_{in}/2$. D_1 is conducting so that v_{Lm} = $n_pV_o/(2n_s)$.

Mode 2 [t_1 ~ t_2]: if $f_{r,1} > f_{sw}$, the i_{D1} will be decreased to 0 at t_1. Then, D_1 is off.

Mode 3 [t_2 ~ t_3]: at t_2, S_1 and S_3 turn off. Due to $i_{Lr} < i_{Lm}$, the fast recovery diode D_4 becomes forward-biased and v_{Lm} = $-n_pV_o/(2n_s)$. The magnetizing current $i_{Lm}(t_2)$ can be obtained as follows:

$$i_{Lm}(t_2) \approx (V_o n_p)/(8 f_{sw} L_m n_s) \tag{4}$$

The ZVS condition of S_4 and S_2 for the high voltage output region is obtained as follows:

$$i_{Lm}(t_2) \geq V_{in}\sqrt{C_{oss}/(L_m + L_r)} \tag{5}$$

In order to have ZVS operation, the maximum value of L_m for the high voltage output region is given as follows:

$$L_m \leq (V_o n_p t_d)/(8 f_{sw} V_{in} C_{oss} n_s) \tag{6}$$

Mode 4 [t_3 ~ t_4]: at t_3, v_{CS2} = v_{CS4} = 0. D_{S4} and D_{S2} become forward-biased. Due to $i_{Lm} > i_{Lr}$, the fast recovery diode D_4 becomes forward-biased and v_{Lm} = $-n_pV_o/(2n_s)$.

Mode 5 [t_4 ~ t_5]: if $f_{r,1} > f_{sw}$, the i_{D4} will be decreased to 0 at time t_4. Then, D_4 becomes reverse-biased.

Mode 6 [t_5 ~ T_{sw}+t_0]: at time t_5, S_4 and S_2 are turned off. Due to $i_{Lr} > i_{Lm}$ after time t_5, the fast recovery diode D_1 becomes forward-biased and v_{Lm} = $n_pV_o/(2n_s)$. At time t_0 + T_{sw}, v_{CS3} = v_{CS1} = 0.

4. Circuit Analysis

For the design of the resonant converter, a general pulse frequency modulation was selected to generate the PWM signals for all power switches. Power switch S_5 is controlled by using an input voltage comparator to select low (or high) winding turns on the output side under the low (or high) voltage output region. For frequency analysis under frequency modulation, the equivalent AC circuit of the proposed converter on the primary side is given in Figure 6a. In Figure 6a, $V_{in,e}$ and R_e are the equivalent AC input voltage and AC resistor on the primary side, respectively. The voltage $V_{in,e}$ is a square voltage waveform with voltage values of 0 V and $V_{in}/2$. One can obtain the input voltage at fundamental frequency $V_{in,e,f} = V_{in}/(\sqrt{2}\pi)$. Components C_{r1} and C_{r2} are connected in parallel ($C_{r,eq}$ = C_{r1} + C_{r2} = 2C_r) under the equivalent AC resonant tank. For the low voltage output range, the turn-ratio of the isolation transformer is n_p/n_s (S_5 off). However, the transformer turn-ratio is $n_p/(2n_s)$ under the high voltage output range (S_5 on). One can obtain the magnetizing voltage v_{Lm} = $\pm n_pV_o/n_s$ (low voltage output range) or $\pm n_pV_o/(2n_s)$ (high voltage output range). The magnetizing voltage at the fundamental frequency can be obtained as $V_{Lm,f} = 2\sqrt{2}n_pV_o/(n_s\pi)$ (or $\sqrt{2}n_pV_o/(n_s\pi)$) for the low output voltage range (or high output voltage range). The equivalent AC resistor R_e on the primary side is given as follows:

$$\begin{aligned} R_e &= \frac{8(n_p/n_s)^2 R_o}{\pi^2} \text{ (low voltage output)} \\ &\text{or } \frac{2(n_p/n_s)^2 R_o}{\pi^2} \text{ (high voltage output)} \end{aligned} \tag{7}$$

The voltage transfer function between the output and input sides is given in Equation (8) and shown in Figure 6b.

$$\begin{aligned} \left|G\right| &= 1/\sqrt{[\frac{f_n^2-1}{f_n^2}\frac{1}{l_n}+1]^2 + (\frac{f_n^2-1}{f_n})^2 x^2} \\ &= \frac{4n_pV_o}{n_sV_{in}} \text{ (low voltage output) or } \frac{2n_pV_o}{n_sV_{in}} \text{ (high voltage output)} \end{aligned} \tag{8}$$

where $x = \sqrt{L_r/2C_r}/R_e$, $l_n = L_m/L_r$, and $f_n = f_{sw}/f_{r,1}$. From Equation (8), V_o can be obtained as follows:

$$V_o = n_s V_{in}/[4n_p\sqrt{[\frac{f_n^2-1}{f_n^2}\frac{1}{l_n}+1]^2+(\frac{f_n^2-1}{f_n})^2x^2}] \text{ (low voltage output)}$$
$$\text{or } n_s V_{in}/[2n_p\sqrt{[\frac{f_n^2-1}{f_n^2}\frac{1}{l_n}+1]^2+(\frac{f_n^2-1}{f_n})^2x^2}] \text{ (high voltage output)} \quad (9)$$

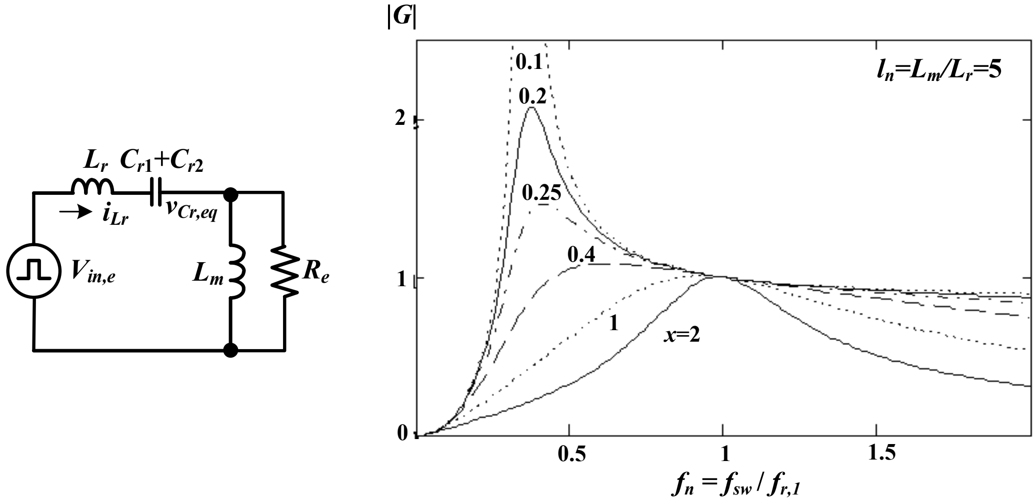

(**a**) (**b**)

Figure 6. Resonant Tank of the proposed converter: (**a**) equivalent AC circuit and (**b**) AC voltage gain.

5. Design Considerations and Experiments

In this presented converter, the following are the basic input and output electric specifications: V_{in} = 760 V, V_o = 50~160 V, P_o = 1000 W, $f_{r,1}$ = 100 *k*Hz, and l_n = 7.5. For the low voltage output range, V_o = 50~90 V. For the high voltage output range, V_o is between 90 and 160 V. The circuit design procedure is based on the low voltage output range (V_o = 50~90 V). The design voltage gain of the presented converter is unity at $f_{sw} = f_{r,1}$ with V_{in} = 760 V and V_o = 50 V. From Equation (8), n_p/n_s can be obtained as follows:

$$\frac{n_p}{n_s} = \frac{V_{in}}{4V_o} = \frac{760}{4 \times 50} \approx 3.8 \quad (10)$$

The transformer *T* is implemented with the ferrite core (TDK EE-55) with A_e = 3.54 cm^2 and ΔB = 0.4 *T*. The assumed minimum switching frequency $f_{sw,min}$ = 60 kHz at V_{in} = 90 V. The primary turns $n_{p,min}$ can be obtained in Equation (11):

$$n_{p,\min} \geq \frac{(n_p/n_s)V_o}{2f_{sw,\min}\Delta B A_e} = \frac{3.8 \times 90}{2 \times 60000\text{Hz} \times 0.4T \times 354 \times 10^{-6}m^2} \approx 20.13 \quad (11)$$

In this laboratory prototype, the selected winding turns were n_p = 32 and n_s = 8. Then, DC voltage gains were obtained through Equations (12) and (13):

$$G_{DC,\max,L} = \frac{4n_p V_{o,\max}}{n_s V_{in}} = \frac{4 \times 32 \times 90}{8 \times 760} \approx 1.89 \quad (12)$$

$$G_{DC,\min,L} = \frac{4n_p V_{o,\min}}{n_s V_{in}} = \frac{4 \times 32 \times 50}{8 \times 760} \approx 1.05 \quad (13)$$

For the high output voltage range (V_o = 90~160 V), the maximum and minimum DC gains of the presented converter could be obtained as follows:

$$G_{DC,\max,H} = \frac{2n_p V_{o,\max}}{n_s V_{in}} = \frac{2 \times 32 \times 160}{8 \times 760} \approx 1.68 \tag{14}$$

$$G_{DC,\min,H} = \frac{2n_p V_{o,\min}}{n_s V_{in}} = \frac{2 \times 32 \times 90}{8 \times 760} \approx 0.95 \tag{15}$$

Under the low output voltage range and the full load condition, R_e is given in Equation (16) at V_o = 90 V:

$$R_e = \frac{8(n_p/n_s)^2 R_o}{\pi^2} = \frac{8 \times (32/8)^2 \times (90^2/1000)}{3.14159^2} \approx 105\Omega \tag{16}$$

The quality factor x = 0.05 and inductor ratio l_n = 7.5 were selected in this design procedure, and C_{r1}, C_{r2}, L_r, and L_m could be derived in Equations (17)–(19).

$$L_r = R_e x/(2\pi f_{r,1}) = (0.05 \times 105)/(2\pi \times 100000) \approx 8.35\mu H \tag{17}$$

$$C_{r1} = C_{r2} = 1/(8\pi^2 L_r f_{r,1}^2) = 1/(8\pi^2 \times 8.35 \times 10^{-6} \times (100000)^2) \approx 152nF \tag{18}$$

$$L_m = L_r \times L_n = 8.35 \times 7.5 \approx 62.6\mu H \tag{19}$$

S_1–S_4 have a voltage stress of 190 V (=$V_{in,max}$/4). STF40N60M2 (650 V/22 A) power devices were selected for S_1–S_4. Die to $V_{o,max}$ = 160 V, STTH15R06D (600 V/12 A) power diodes were selected for D_1–D_4. Power switch S_5 was chosen to be implemented by 6R070P6 (650 V/33 A). The selected capacitances were C_{in1} = C_{in2} = 330 µF/450 V and C_o = 1360 µF/200 V. The Schmitt voltage comparator with V_f = 90 V was selected to control switch S_5 (S_5 OFF if $V_o \leq 90$ V or S_5 ON if $V_o > 90$ V). The UCC25600 was selected to implement pulse frequency modulation for S_1–S_4. Table 1 illustrates the circuit parameters in the laboratory prototype. Figure 7 shows a picture of the prototype circuit in the laboratory test.

Table 1. Circuit components in the prototype circuit.

Items.	Parameter	Items	Parameter
V_{in}	760 V	V_o	50~160 V
P_o	1 kW	S_1~S_4	STF40N60M2 (650 V/22 A)
C_{in1}, C_{in2}	330 µF/450 V	D_1~D_4	STTH15R06D (600 V/12 A)
$f_{r,1}$	100 kHz	S_5	6R070P6 (650 V/33 A)
C_o	1360 µF/200 V	n_p:n_s	32:8
L_r	8.35 µH	L_m	62.6 µH
C_{r1}, C_{r2}	152 nF		

Figure 7. Picture of the prototype circuit in the laboratory test.

The experimental results of the proposed converter for low voltage range operation are illustrated in Figures 8 and 9. Figure 8 illustrates the experiments of the presented circuit under V_{in} = 760 V and V_o = 50 V at a 1 kW load. Figure 8a gives the experimental PWM waveforms of S_1–S_4. S_1 and S_3 were found to have the same PWM signals. In the same manner, the PWM signals of S_2 and S_4 were identical. Figure 8b shows the PWM signal of S_1 and leg voltages v_{ab} and v_{bc}. If S_1 and S_3 were on and S_2 and S_4 were off, then the leg voltages $v_{ab} = V_{Cdc1} = V_{in}/2$ = 380 V and $v_{bc} = 0$. When S_1 and S_3 were off and S_2 and S_4 were on, the leg voltages $v_{ab} = 0$ and $v_{bc} = V_{Cdc2} = V_{in}/2$ = 380 V. Figure 8c illustrates the experimental waveforms of v_{Cr1}, v_{Cr2}, and i_{Lr}. The AC voltage components of v_{Cr1} and v_{Cr2} were found to be complementary to each other, and the voltage value $v_{Cr1} + v_{Cr2} = V_{in}/2$. Due to the half bridge type resonant circuit, the DC voltage values $v_{Cr1,DC} = v_{Cr2,DC} = V_{in}/4$ = 190 V. The presented converter at V_o = 50 V had a $G_{DC,min,L}$ = 1.05 theoretical DC voltage gain. The switching frequency was close to the resonant frequency. Therefore, the inductor current i_{Lr} was a sinusoidal waveform. Since the presented converter at V_o = 50 V was operated under the low voltage output region, S_5 was off and D_1 and D_4 were reverse-biased. Figure 8d illustrates the experimental waveforms of the secondary-side currents i_{D2}, i_{D3}, and I_o and load voltage V_o. The PWM signals of S_1 at P_o = 200 W (20% load) and 1 kW (100% load) are given in Figure 8e,f, respectively. It can be seen in Figure 8e,f that the active device S_1 turned on at ZVS from 20% load to 100% load. In the same manner, the experiments of the presented converter under V_o = 90 V and 1 kW load are illustrated in Figure 9. Following from Equations (12) and (13), the converter at V_o = 90 V output had more voltage gain than at the V_o = 50 V output condition. Thus, the switching frequency in Figure 9a–d (at V_o = 90 V output) was less than the switching frequency in Figure 8a–d (at V_o = 50 V output). For V_o = 90 V output, the theoretical DC voltage gain in Equation (12) was 1.89. Therefore, it could be expected that the switching frequency was less than the series resonant frequency shown in Figure 9c and the fast recovery diodes D_2 and D_3 could be turned off at the zero current switching shown in Figure 9d. From the experiments shown in Figure 9e,f, it is clear that S_1 turned on at ZVS from 20% load to 100% load. Similarly, the experiments of the converter under high voltage range operation are provided in Figures 10 and 11. For the high voltage output operation, S_5 was on and D_2 and D_3 were reverse-biased. Figures 10 and 11 illustrate the experiments for the V_o = 95 and 160 V output and 100% load conditions. Following Equations in (14) and (15), the voltage gain of converter at V_o = 95 V was close to unity and the DC voltage gain at V_o = 160 V was greater than unity. Therefore, the switching frequency of the presented converter at the V_o = 95 V (160 V) output was greater (less) than the resonant frequency. This phenomenon can be observed in Figures 10a–d and 11a–d. For the V_o = 95 V condition, it can be seen that $f_{sw} > f_{r,1}$. In Figure 10d, the fast recovery diodes D_1 and D_4 were turned off at hard switching. On the other hand, the switching frequency $f_{sw} < f_{r,1}$ under the V_o = 160 V output condition. Therefore, D_1 and D_4 were turned off at zero current switching, as shown in Figure 11d. From the test experiments in Figure 10e,f and Figure 11e,f, it can be seen that S_1 was turned off at ZVS from 20% load to full load for both V_o = 95 and 160 V. Since the circuit characteristics of S_2, S_3, and S_4 are the same as S_1, it could be expected that S_1–S_4 had the soft switching turn-on operation. The experiments of output voltage V_o and switch S_5 are provided in Figure 12 during the output voltage variation between 50 and 160 V. If the output voltage was less than 90 V, S_5 was off ($v_{S5,g}$ = 0 V). On the other hand, S_5 was on ($v_{S5,g}$ = 15 V) if V_o > 90 V. The presented converter had 90%, 94%m and 91% efficiencies at V_o = 50, 95, and 160 V, respectively, under the V_{in} = 760 V and P_o = 1 kW conditions. The proposed converter at V_o = 95 V was operated at $f_{sw} > f_{r,1}$. Therefore, power switches were operated at ZVS turn-on and rectifier diodes were operated at hard switching turn-off. Due to the $f_{sw} > f_{r,1}$ at the V_o = 95 V condition, the higher switching frequency reduced the magnetizing current loss compared to the V_o = 160 V condition ($f_{sw} < f_{r,1}$). Therefore, the circuit efficiency at the V_o = 95 V condition was better than V_o = 160 V.

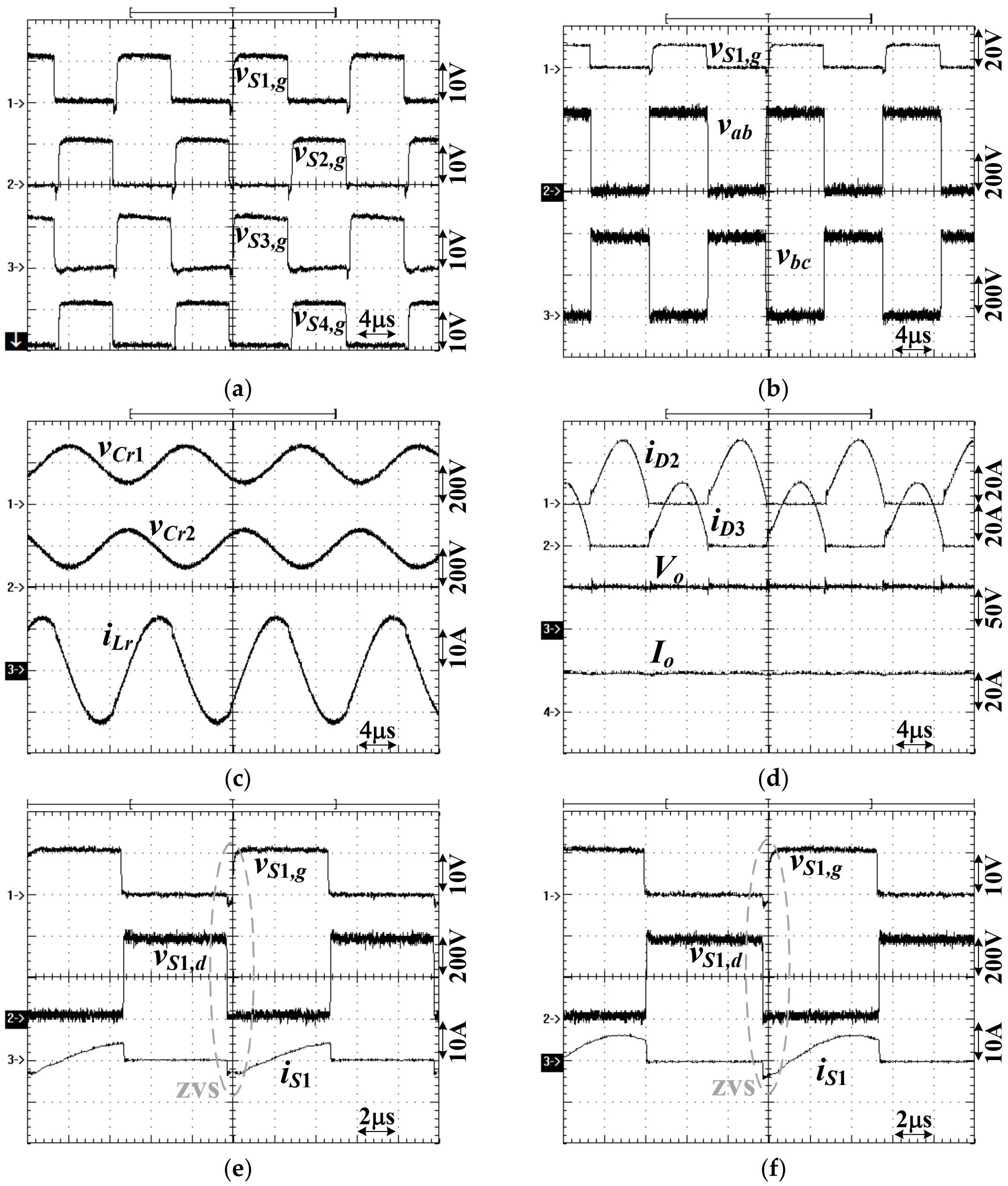

Figure 8. Experiments of the presented converter under V_o = 50 V: (**a**) $v_{S1,g}$, $v_{S2,g}$, $v_{S3,g}$, and $v_{S4,g}$ under V_{in} = 760 V and P_o = 1 kW; (**b**) $v_{S1,g}$, v_{ab}, and v_{bc} under V_{in} = 760 V and P_o = 1 kW; (**c**) v_{Cr1}, v_{Cr2}, and i_{Lr} under V_{in} = 760 V and P_o = 1 kW; (**d**) i_{D2}, i_{D3}, V_o, and I_o under V_{in} = 760 V and P_o = 1 kW; (**e**) $v_{S1,g}$, $v_{S1,d}$, and i_{S1} under V_{in} = 760 V and P_o = 200 W; and (**f**) $v_{S1,g}$, $v_{S1,d}$, and i_{S1} under V_{in} = 760 V and P_o = 1 kW.

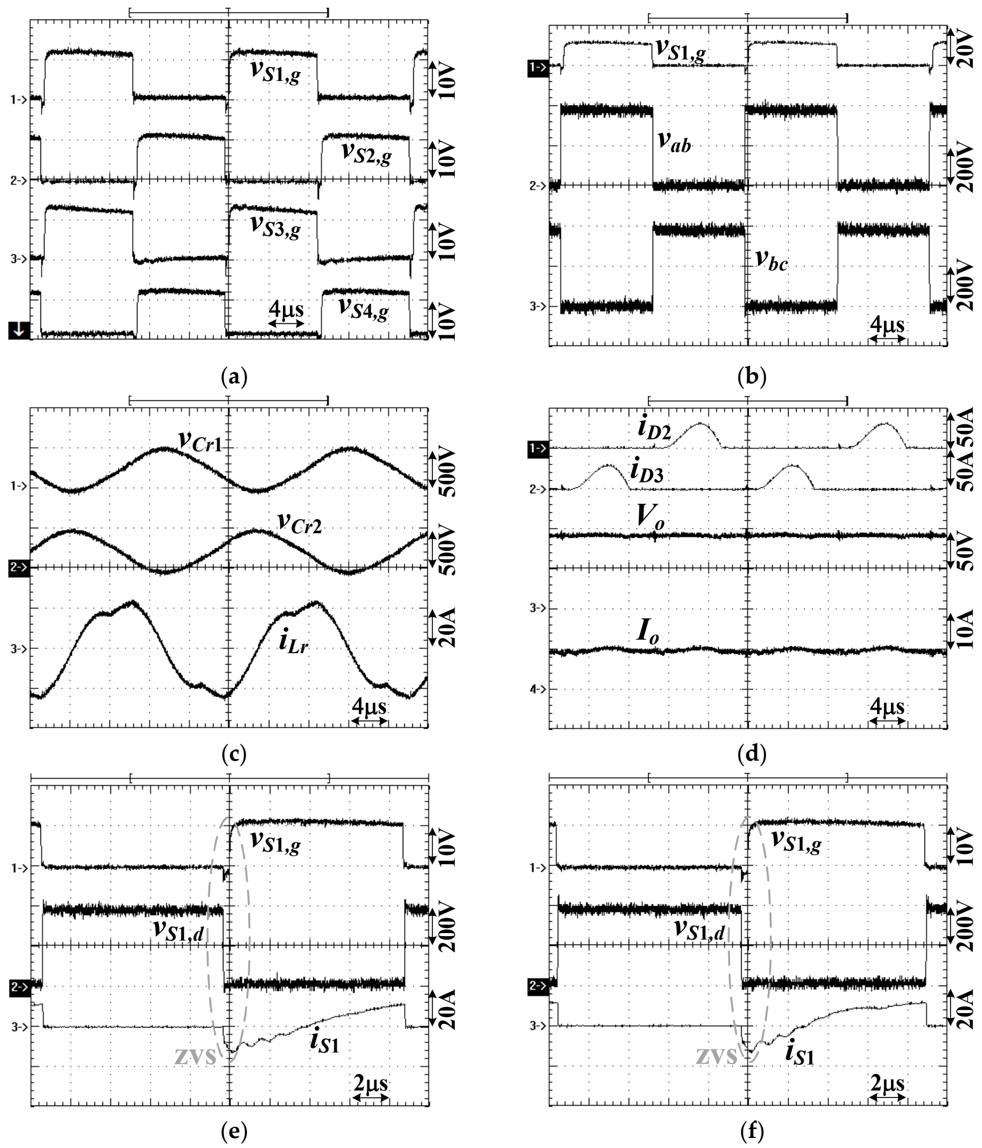

Figure 9. Experiments of the presented converter under V_o = 90 V: (**a**) $v_{S1,g}$, $v_{S2,g}$, $v_{S3,g}$, and $v_{S4,g}$ under V_{in} = 760 V and P_o = 1 kW; (**b**) $v_{S1,g}$, v_{ab}, and v_{bc} under V_{in} = 760 V and P_o = 1 kW; (**c**) v_{Cr1}, v_{Cr2}, and i_{Lr} under V_{in} = 760 V and P_o = 1 kW; (**d**) i_{D2}, i_{D3}, V_o, and I_o under V_{in} = 760 V and P_o = 1 kW; (**e**) $v_{S1,g}$, $v_{S1,d}$, and i_{S1} under V_{in} = 760 V and P_o = 200 W; and (**f**) $v_{S1,g}$, $v_{S1,d}$, and i_{S1} under V_{in} = 760 V and P_o = 1 kW.

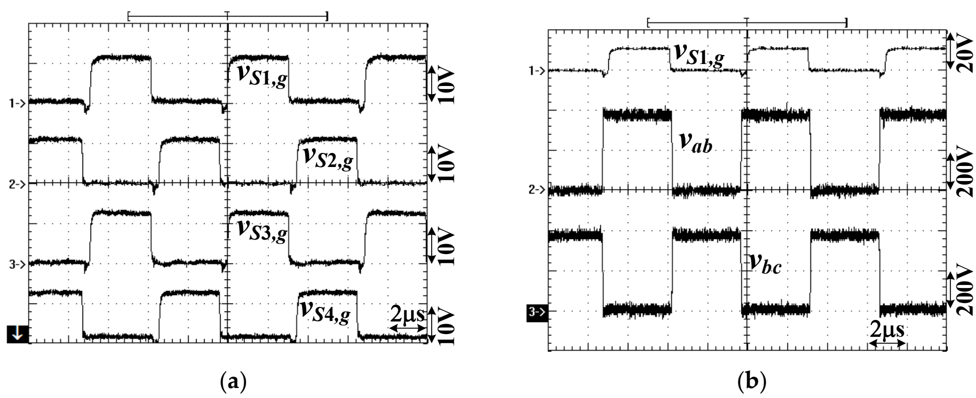

Figure 10. *Cont*.

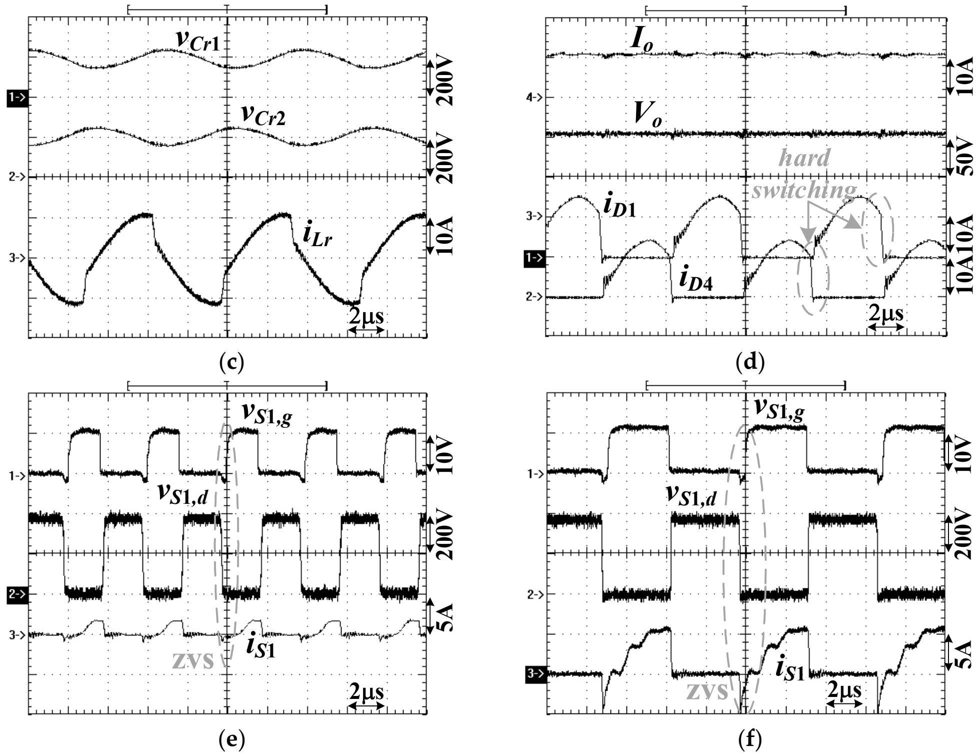

Figure 10. Experiments of the presented converter under V_o = 95 V: (**a**) $v_{S1,g}$, $v_{S2,g}$, $v_{S3,g}$, and $v_{S4,g}$ under V_{in} = 760 V and P_o = 1 kW; (**b**) $v_{S1,g}$, v_{ab}, and v_{bc} under V_{in} = 760 V and P_o = 1 kW; (**c**) v_{Cr1}, v_{Cr2}, and i_{Lr} under V_{in} = 760 V and P_o = 1 kW; (**d**) I_o, V_o, i_{D1}, and i_{D4} under V_{in} = 760 V and P_o = 1 kW; (**e**) $v_{S1,g}$, $v_{S1,d}$, and i_{S1} under V_{in} = 760 V and P_o = 200 W; and (**f**) $v_{S1,g}$, $v_{S1,d}$, and i_{S1} under V_{in} = 760 V and P_o = 1 kW.

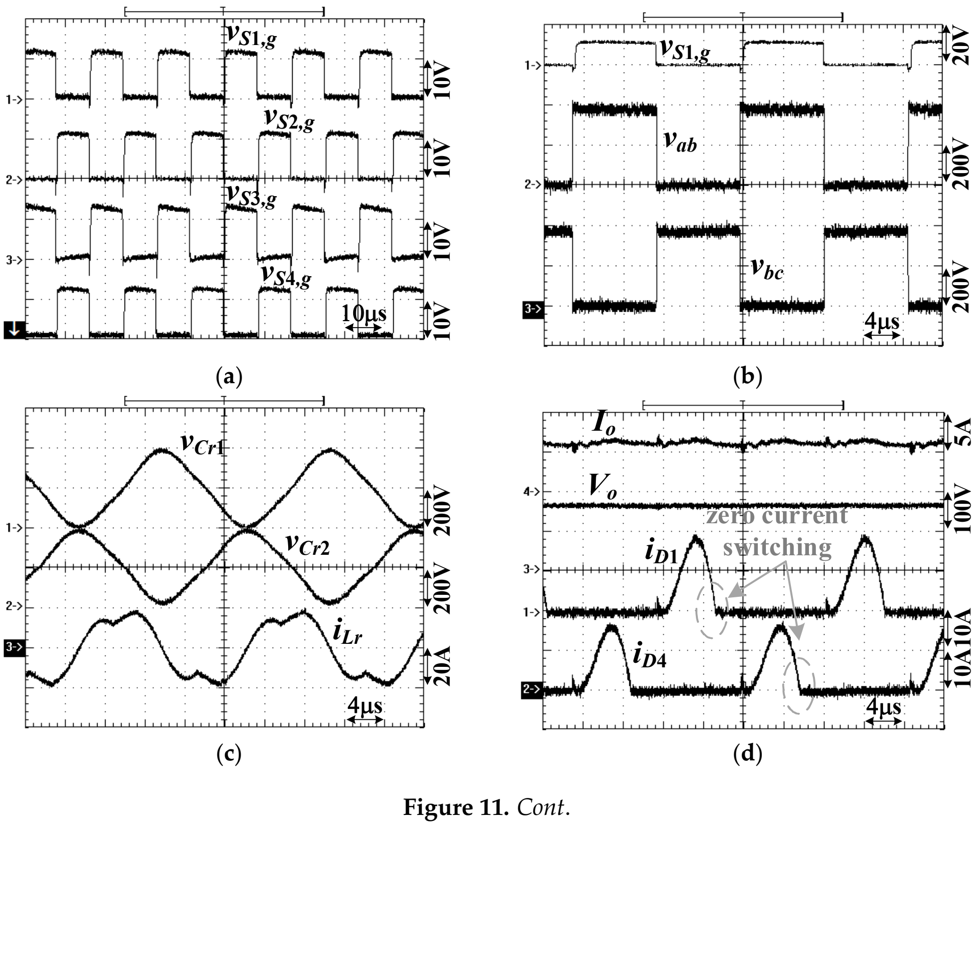

Figure 11. *Cont.*

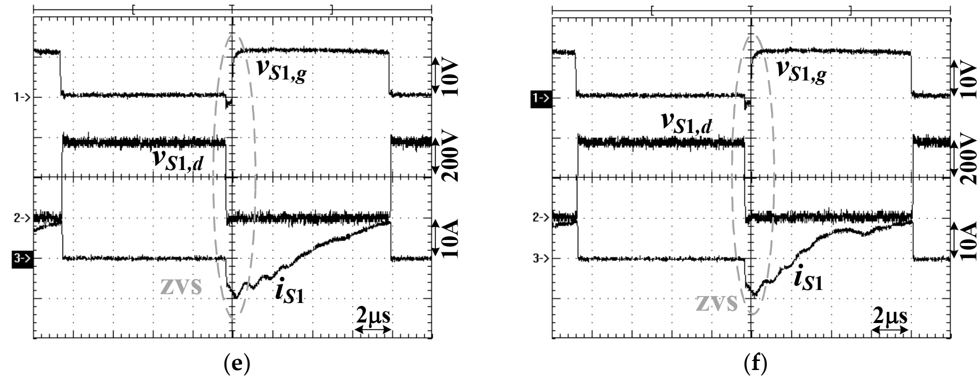

Figure 11. Experiments of the presented converter under V_o = 160 V: (**a**) $v_{S1,g}$, $v_{S2,g}$, $v_{S3,g}$, and $v_{S4,g}$ under V_{in} = 760 V and P_o = 1 kW; (**b**) $v_{S1,g}$, v_{ab}, and v_{bc} under V_{in} = 760 V and P_o = 1 kW; (**c**) v_{Cr1}, v_{Cr2}, and i_{Lr} under V_{in} = 760 V and P_o = 1 kW; (**d**) I_o, V_o, i_{D1}, and i_{D4} under V_{in} = 760 V and P_o = 1 kW; (**e**) $v_{S1,g}$, $v_{S1,d}$, and i_{S1} under V_{in} = 760 V and P_o = 200 W; and (**f**) $v_{S1,g}$, $v_{S1,d}$, and i_{S1} under V_{in} = 760 V and P_o = 1 kW.

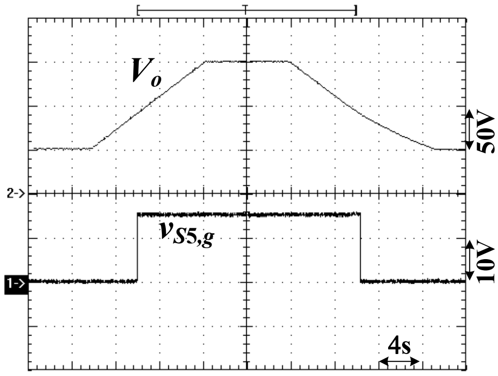

Figure 12. Experiments of V_o and I_o during output voltage variation between 50 and 160 V.

6. Conclusions

A new DC resonant converter is presented and verified in this paper in DC nano- or micro-grid systems with a wide output voltage capability. The main contributions of the presented DC–DC converter are (1) a high input voltage circuit structure that uses a flying capacitor to balance two input capacitor voltages, (2) a wide output voltage operation using a control switch, and (3) a wide ZVS operation range for wide output voltage and load ranges. Since the square voltage waveforms are generated on v_{ab} and v_{bc}, the voltage v_{Cr1} + v_{Cr2} = V_{Cdc1} (if S_1 and S_3 are on) with $d = T_{sw}/2$ or V_{Cdc2} (if S_2 and S_4 are on) with $d = T_{sw}/2$. Thus, the flying capacitors C_{r1} and C_{r2} can be used to balance input capacitor voltages $V_{Cdc1} = V_{Cdc2} = V_{in}/2$. To solve the high voltage application problems, a cascade resonant circuit is used on high voltage side to limit the voltage stress on active devices at $V_{in}/2$. Therefore, the general purpose power MOSFETs with a 600 V voltage rating can be used in the presented circuit. To realize wide output voltage requirements, such as for battery chargers for universal electric motorcycles or vehicles, the converter has two winding sets to extend the output voltage range using a control switch. In order to lessen the switching losses on active devices and increase the circuit efficiency, a series resonant converter using a *LLC* circuit structure was adopted for the presented converter to have a ZVS turn-on characteristic on active devices and a possible ZCS turn-off characteristic on fast recovery diodes. Therefore, the proposed converter can achieve soft switching operation from 200 to 1000 W load in the experimental test. Finally, the design procedures and experiments of the prototype circuit are provided to show the circuit performance and effectiveness of the studied converter. Further work on this circuit will consider reducing the number of circuit components and cost, as well as extending the output voltage range for universal battery charging station applications.

Funding: This research is supported by the Ministry of Science and Technology (MOST), Taiwan, under grant number MOST 108-2221-E-224-022-MY2.

Acknowledgments: The author thanks the financial support by the Ministry of Science and Technology, Taiwan, under contract MOST 108-2221-E-224-022-MY2. The author also likes to thank Y.H. Peng for his help to measure and validate the experimental waveforms.

Conflicts of Interest: The author declare no conflict of interest.

References

1. He, J.; Yang, Y.; Vinnikov, D. Energy Storage for 1500 V Photovoltaic Systems: A Comparative Reliability Analysis of DC- and AC-Coupling. *Energies* **2020**, *13*, 3355. [CrossRef]
2. Youssef, E.; Costa, P.B.C.; Pinto, S.F.; Amin, A.; El Samahy, A.A. Direct Power Control of a Single Stage Current Source Inverter Grid-Tied PV System. *Energies* **2020**, *13*, 3165. [CrossRef]
3. Yang, M.; Cao, W.; Lin, T.; Zhao, J.; Li, W. Low Frequency Damping Control for Power Electronics-Based AC Grid Using Inverters with Built-In PSS. *Energies* **2021**, *14*, 2435. [CrossRef]
4. Ali, A.I.M.; Sayed, M.A.; Mohamed, A.A.S. Seven-Level Inverter with Reduced Switches for PV System Supporting Home-Grid and EV Charger. *Energies* **2021**, *14*, 2718. [CrossRef]
5. Frivaldsky, M.; Morgos, J.; Prazenica, M.; Takacs, K. System Level Simulation of Microgrid Power Electronic Systems. *Electronics* **2021**, *10*, 644. [CrossRef]
6. Zhang, C.; Li, P.; Guo, Y. Bidirectional DC/DC and SOC Drooping Control for DC Microgrid Application. *Electronics* **2020**, *9*, 225. [CrossRef]
7. Litrán, S.P.; Durán, E.; Semião, J.; Barroso, R.S. Single-Switch Bipolar Output DC-DC Converter for Photovoltaic Application. *Electronics* **2020**, *9*, 1171. [CrossRef]
8. Xiong, X.; Yang, Y. A Photovoltaic-Based DC Microgrid System: Analysis, Design and Experimental Results. *Electronics* **2020**, *9*, 941. [CrossRef]
9. Thayumanavan, P.; Kaliyaperumal, D.; Subramaniam, U.; Bhaskar, M.S.; Padmanaban, S.; Leonowicz, Z.; Mitolo, M. Combined Harmonic Reduction and DC Voltage Regulation of a Single DC Source Five-Level Multilevel Inverter for Wind Electric System. *Electronics* **2020**, *9*, 979. [CrossRef]
10. Kim, D.H.; Kim, M.S.; Nengroo, S.H.; Kim, C.H.; Kim, H.J. LLC Resonant Converter for LEV (Light Electric Vehicle) Fast Chargers. *Electronics* **2019**, *8*, 362. [CrossRef]
11. Mouli, G.R.C.; Duijsen, P.V.; Grazian, F.; Jamodkar, A.; Bauer, P.; Isabella, O. Sustainable E-Bike Charging Station That Enables AC, DC and Wireless Charging from Solar Energy. *Energies* **2020**, *13*, 3549. [CrossRef]
12. Kim, C.-E. Optimal Dead-Time Control Scheme for Extended ZVS Range and Burst-Mode Operation of Phase-Shift Full-Bridge (PSFB) Converter at Very Light Load. *IEEE Trans. Power Electron.* **2019**, *34*, 10823–10832. [CrossRef]
13. Jain, P.; Pahlevaninezhad, M.; Pan, S.; Drobnik, J. A Review of High-Frequency Power Distribution Systems: For Space, Telecommunication, and Computer Applications. *IEEE Trans. Power Electron.* **2014**, *29*, 3852–3863. [CrossRef]
14. Madhusoodhanan, S.; Tripathi, A.; Patel, D.; Mainali, K.; Kadavelugu, A.; Hazra, S.; Bhattacharya, S.; Hatua, K. Solid-State Transformer and MV Grid Tie Applications Enabled by 15 kV SiC IGBTs and 10 kV SiC MOSFETs Based Multilevel Converters. *IEEE Trans. Ind. Appl.* **2015**, *51*, 3343–3360. [CrossRef]
15. Lin, B.-R.; Lu, H.-H. New multilevel rectifier based on series connection of H-bridge cell. *IEE Proc. Electr. Power Appl.* **2000**, *147*, 304. [CrossRef]
16. Duarte, J.L.; Lokos, J.; Van Horck, F.B.M. Phase-Shift-Controlled Three-Level Converter with Reduced Voltage Stress Featuring ZVS Over the Full Operation Range. *IEEE Trans. Power Electron.* **2012**, *28*, 2140–2150. [CrossRef]
17. Lin, B.-R.; Chao, C.-H. A New ZVS DC/DC Converter with Three APWM Circuits. *IEEE Trans. Ind. Electron.* **2012**, *60*, 4351–4358. [CrossRef]
18. Pont, N.C.D.; Bandeira, D.G.; Lazzarin, T.B.; Barbi, I. A ZVS APWM Half-Bridge Parallel Resonant DC–DC Converter with Capacitive Output. *IEEE Trans. Ind. Electron.* **2019**, *66*, 5231–5241. [CrossRef]
19. Ren, R.; Liu, B.; Jones, E.A.; Wang, F.F.; Zhang, Z.; Costinett, D. Capacitor-Clamped, Three-Level Gan-Based dc-dc Converter with Dual Voltage Outputs for Battery Charger Applications. *IEEE J. Emerg. Sel. Top. Power Electron.* **2016**, *4*, 841–853. [CrossRef]
20. Safaee, A.; Jain, P.; Bakhshai, A. A ZVS Pulsewidth Modulation Full-Bridge Converter with a Low-RMS-Current Resonant Auxiliary Circuit. *IEEE Trans. Power Electron.* **2015**, *31*, 4031–4047. [CrossRef]
21. Steigerwald, R.L. A comparison of half-bridge resonant converter topologies. *IEEE Trans. Power Electron.* **1988**, *3*, 174–182. [CrossRef]
22. Lin, B.; Chu, C. Hybrid full-bridge and LLC converter with wide ZVS range and less output inductance. *IET Power Electron.* **2016**, *9*, 377–384. [CrossRef]